Article

The Effects of Chlorine Doping on the Thermoelectric Properties of Bi_2O_2Se

Buda Li [1], Menglu Li [2], Hangbo Qi [2], Xiaotao Zu [2], Liang Qiao [2,*] and Haiyan Xiao [1,*]

[1] Yangtze Delta Region Institute (Huzhou), University of Electronic Science and Technology of China, Huzhou 313001, China; libuda66@163.com

[2] School of Physics, University of Electronic Science and Technology of China, Chengdu 611731, China; mengluli0121@163.com (M.L.); qihangbo@u.nus.edu (H.Q.); xtzu@uestc.edu.cn (X.Z.)

* Correspondence: liang.qiao@uestc.edu.cn (L.Q.); hyxiao@uestc.edu.cn (H.X.)

Abstract: In this study, we investigate the effects of chlorine doping on the structural, electronic, and thermoelectric properties of Bi_2O_2Se by employing density functional theory combined with semiclassical Boltzmann transport theory. It is shown that chlorine doping has significant effects on the electronic structure and thermoelectric properties of Bi_2O_2Se. As chlorine is incorporated into the selenium sites in Bi_2O_2Se, additional electrons are acquired, thereby inducing metallic properties in chlorine-doped Bi_2O_2Se. Meanwhile, Cl doping leads to an increase in the electrical conductivity of Bi_2O_2Se at room temperature by 25 times (from 358.59 S/cm to 9390 S/cm), and the power factor is enhanced by a factor of 2.12 (from 4.04 mW/mK^2 to 12.59 mW/mK^2). This study demonstrates that chlorine doping is an effective method to modify the physical properties of Bi_2O_2Se.

Keywords: density functional theory; Bi_2O_2Se; chlorine doping; electronic structure; thermoelectric properties

1. Introduction

In recent years, thermoelectric (TE) materials have received extensive attention because of their environmentally friendly and sustainable characteristics. Thermoelectric materials can directly convert heat into electricity, thus reducing carbon dioxide and greenhouse gas emissions [1–6]. The energy conversion efficiency of thermoelectric materials can be evaluated using the ZT ($ZT = T\frac{S^2\sigma}{\kappa}$) value [7,8], where σ, S, T, κ and $S^2\sigma$ are the electrical conductivity, Seebeck coefficient, absolute temperature, thermal conductivity, and power factor, respectively [9–12]. Excellent thermoelectric materials should have a high Seebeck coefficient, high electrical conductivity, and low thermal conductivity [5]. However, these parameters are strongly coupled; e.g., the electrical conductivity is proportional to the thermal conductivity, while the carrier concentration is inversely proportional to the Seebeck coefficient. Thus, it is difficult to further improve the ZT value of TE materials.

Bismuth oxyselenide (Bi_2O_2Se) is a potential thermoelectric material due to its low thermal conductivity; however, its ZT value (0.05~0.5) is lower than that of other thermoelectric materials (~1) [13–18]. In the past decades, many techniques have been employed to improve the ZT value of Bi_2O_2Se. Experimental studies performed by Zhan et al. have shown that Bi defects significantly influence the thermoelectric performance of Bi_2O_2Se. Compared to the ZT value of 0.05 for pure Bi_2O_2Se, $Bi_{1.9}O_2Se$ exhibits a 130% improvement in ZT value, reaching 0.12 at 773 K [19]. Guo et al. investigated the effect of Nb doping on the ZT value of Bi_2O_2Se using ball milling and hot-pressing sintering. They found that Nb-doped Bi_2O_2Se has a ZT value of 0.195 at 823 K, which is 325% higher than the value of 0.045 for pure Bi_2O_2Se [20]. Hong et al. studied the influence of Ce^{4+} doping on the thermoelectric properties of Bi_2O_2Se employing spark plasma sintering and found that Ce^{4+}-doped Bi_2O_2Se has a ZT value of 0.26 at 773 K, which is 1.27 times higher than the value of 0.11 for pure Bi_2O_2Se [21]. Song et al. studied the influence of Ti doping on the

thermoelectric properties of Bi_2O_2Se and found that the *ZT* value of Ti-doped Bi_2O_2Se is 0.56 at 773 K, which is 20% higher than the *ZT* value of 0.47 for the original Bi_2O_2Se [22]. Chen et al. investigated the effect of Sb doping on the thermoelectric properties of Bi_2O_2Se and found that the *ZT* value of Sb-doped Bi_2O_2Se reaches 0.59 at 773 K, which is 80% higher than that of 0.33 for the original Bi_2O_2Se [23]. Pan et al. synthesized polycrystalline $Bi_2O_{2-x}S_xSe$ (x = 0, 0.01, 0.02, and 0.03) via a high-temperature solid-state reaction and demonstrated that the substitution of a small amount of S for O can effectively improve the thermoelectric performance of Bi_2O_2Se. The doped Bi_2O_2Se exhibits a *ZT* value of 0.29, which is 3.2 times higher than that of 0.09 for pristine Bi_2O_2Se at 793 K [24]. Fu et al. synthesized $Bi_{2-x}Zr_xO_2Se$ (x = 0, 0.02, 0.04, 0.06) via a combination of high-energy ball milling and cold pressing. It was found that Zr doping has a significant impact on the thermoelectric performance of Bi_2O_2Se. The peak *ZT* value of the $Bi_{1.96}Zr_{0.04}O_2Se$ sample is approximately 0.27, which is 2.4 times higher than that of the undoped sample (~0.11) [25]. Song et al. obtained Bi_2O_2Se with $Bi_2Te_{2.7}Se_{0.3}$ through a liquid-assisted shear exfoliation-reassembly (LASE-R) process and found a significant improvement in its thermoelectric performance. At 772 K, the addition of 0.3 mol% $Bi_2Te_{2.7}Se_{0.3}$ results in a *ZT* value of 0.7, several times higher than the pristine sample (~0.1) [26]. Despite the above studies, the *ZT* value of Bi_2O_2Se remains low and requires further improvement.

In recent years, chlorine (Cl) has been widely used to improve the thermoelectric properties of materials [27–29]. Tan et al. experimentally studied the effect of Cl doping on the thermoelectric performance of $AgBi_3S_5$. They found that the *ZT* value of Cl-doped $AgBi_3S_5$ reaches 1 at 800 K, which is five times that of the original $AgBi_3S_5$ (0.2) [28]. Zhang et al. systematically studied the effect of Cl doping on the thermoelectric properties of $AgPb_{18}SbSe_{20}$ using experimental methods. It was shown that the *ZT* value of Cl-doped $AgPb_{18}SbSe_{20}$ is 1.3 at 873 K, which is 766% higher than that of the original $AgPb_{18}SbSe_{20}$ (0.15) [29]. Furthermore, Wang et al. carried out experimental investigations of the effect of Cl doping on the thermoelectric properties of $BiSbSe_3$ and reported that the *ZT* value of Cl-doped $BiSbSe_3$ is 1.0 at 800 K, which is five times higher than that of the original $BiSbSe_3$ (0.2) [27]. These investigations demonstrate that Cl doping is an effective method to improve the thermoelectric properties of materials.

In this work, the effects of Cl doping on the structure, electronic, and thermoelectric properties of Bi_2O_2Se are investigated by combining the DFT method and semi-classical Boltzmann transport theory. The relaxation time τ, electrical conductivity σ, Seebeck coefficient S, power factor (*PF*), thermal conductivity κ, and dimensionless figure of merit *ZT* are provided. The results show that Cl doping can introduce additional electrons, causing Bi_2O_2Se to exhibit metallic character, thus enhancing the electrical conductivity and power factor. Therefore, this study provides a theoretical basis for experimental observation and reveals the potential mechanism of Cl-doping-induced improvement in the thermoelectric properties of Bi_2O_2Se.

2. Computational Details

The density functional theory (DFT) method in the Vienna Ab initio Simulation Package (VASP) code (Vienna, Austria) [30] is used to perform geometrical optimization and electronic structure calculations. The projector augmented-wave approach (PAW) [31] pseudopotential is used to describe the interaction between electrons and ions. In addition, the exchange-correlation potentials among electrons are described by the Perdew–Burke–Ernzerhof (PBE) functional within the generalized gradient approximation (GGA) [32] and the Heyd–Scuseria–Ernzerhof (HSE06) hybrid functional [33]. In this work, the Monkhorst–Pack scheme [34] with a $6 \times 6 \times 6$ k-point sampling for the Brillouin zone is used for structural optimization and electronic structure calculations. The cut-off energy of the plane waves is set as 500 eV. The electronic transport coefficients are calculated by semi-classical Boltzmann theory using the BOLTZTRAP code [35] and the Brillouin zone is sampled with an $8 \times 8 \times 8$ k-point grid. The lattice thermal conductivity κ_l is calculated by using the Slack equation [36], and the energy and force convergence criteria are set

to be 1×10^{-5} eV/atom and 1×10^{-2} eV/Å, respectively. For chemical element doping, a $2 \times 2 \times 1$ supercell containing 40 atoms is used to build the structural model for $Bi_2O_2Se_{0.875}Cl_{0.125}$, with Cl dopants substituting for the Se atoms. It should be pointed out that the doping concentration in this work is 1.31×10^{21} e/cm³, which may exceed the saturation limit. The dissolution limit can be raised by tuning experimental conditions, such as the experimental temperature and powder size of the samples [37–39]. On the other hand, in the literature, Liu et al. have demonstrated that the carrier concentration of Ge-doped Bi_2O_2Se can reach 10^{21}–10^{22} cm⁻³ by controlling experimental conditions [40]. Therefore, the doping concentration of 1.31×10^{21} e/cm³ can probably be achieved experimentally.

3. Results and Discussions

3.1. Structural Properties of Pristine and Cl-Doped Bi_2O_2Se

The bent $[Bi_2O_2]^{2+}$ layers and $[Se]^{2-}$ layers are alternately stacked along the c-axis through weak electrostatic interactions to form Bi_2O_2Se [41], in which the $[Bi_2O_2]^{2+}$ layer is an insulating layer while the $[Se]^{2-}$ layer is a conducting layer. Bulk Bi_2O_2Se has a tetragonal I4/mmm (No. 139) crystal structure, and its unit cell contains ten atoms. The optimized geometrical structures of Bi_2O_2Se and $Bi_2O_2Se_{0.875}Cl_{0.125}$ are shown in Figure 1, and both structures contain 40 atoms. Table 1 shows the lattice constants, volume, and bond lengths of Bi_2O_2Se and $Bi_2O_2Se_{0.875}Cl_{0.125}$ calculated by us and from other literature sources [42,43]. The lattice constants of Bi_2O_2Se are $a_0 = b_0 = 3.917$ Å and $c_0 = 12.357$ Å, which are in good agreement with experimental results ($a_0 = b_0 = 3.88$ Å and $c_0 = 12.16$ Å) [42] as well as calculated results ($a_0 = b_0 = 3.90$ Å and $c_0 = 12.39$ Å) [43] reported in the literature. Additionally, the calculated <Bi-O> and <Bi-Se> bond lengths of Bi_2O_2Se are 2.337 Å and 3.331 Å, respectively, which agree well with the calculated values of 2.312 Å and 3.272 Å reported by Wu et al. [44]. Compared with Bi_2O_2Se, the calculated lattice constants a_0 and b_0 (3.946 Å) of $Bi_2O_2Se_{0.875}Cl_{0.125}$ increased by 0.74%, respectively, while the c_0 (12.287 Å) decreased by 0.57%, resulting in a 0.76% increase in volume. The calculated <Bi-O> bond length (2.339 Å) of $Bi_2O_2Se_{0.875}Cl_{0.125}$ increased by 0.09%, and <Bi-Se> bond length (3.336 Å) increased by 0.76%. As Cl substitutes for Se in Bi_2O_2Se, despite the smaller ionic radii of Cl (1 Å) compared to Se (1.15 Å), the stronger electronegativity (3.16) of the Cl atom than Se (2.55) results in the attraction of electrons from its neighboring atoms. Consequently, the interactions between Bi atoms and O as well as Se atoms are weakened, as indicated by the increased bond lengths of <Bi-O> and <Bi-Se> by 0.09% and 0.76%, respectively (see Table 1). This probably eventually leads to the volume expansion of 0.9% caused by Cl doping in Bi_2O_2Se. Considering that Cl and Se atoms have 7 and 6 valence electrons, respectively, when Cl is used to substitute for Se, it is likely that one additional electron is introduced.
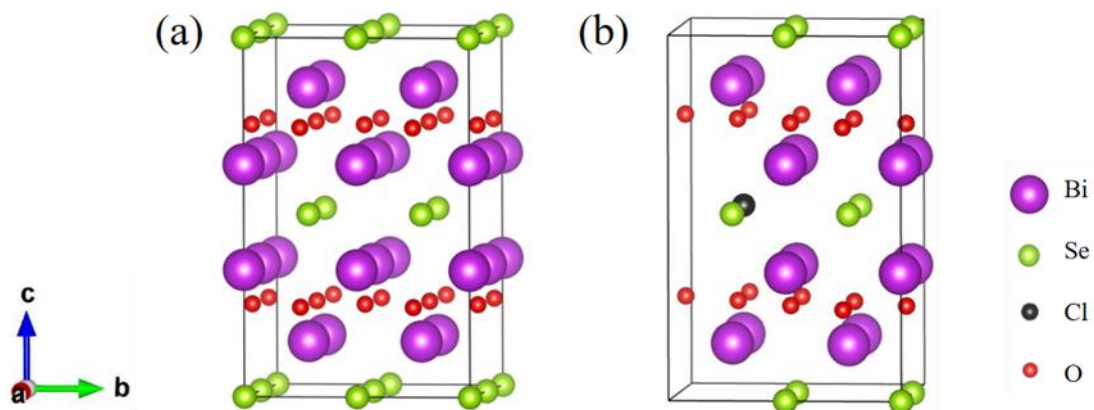

Figure 1. The structure of (**a**) Bi_2O_2Se and (**b**) $Bi_2O_2Se_{0.875}Cl_{0.125}$. The purple, green, black, and red spheres denote Bi, Se, Cl, and O atoms, respectively.

Table 1. Comparison of lattice constants a_0 and c_0 (Å), volume (Å³), and bond length (Å) of Bi_2O_2Se and $Bi_2O_2Se_{0.875}Cl_{0.125}$ with experimental and other theoretical results.

		a_0	c_0	Volume	<Bi-O>	<Bi-Se>
Bi_2O_2Se	Our cal.	3.917	12.357	189.592	2.337	3.311
	Exp. [42]	3.88	12.16	183.06	---	---
	Other cal. [43]	3.90	12.39	188.45	---	---
$Bi_2O_2Se_{0.875}Cl_{0.125}$	Our cal.	3.946	12.287	191.320	2.339	3.336

3.2. The Influence of Cl Doping on the Electronic Structure of Bi_2O_2Se

The density of state (DOS) distribution of Bi_2O_2Se before and after Cl doping is first studied using standard and hybrid DFT methods. Figure 2a,b show the total and projected density of state distribution of Bi_2O_2Se and $Bi_2O_2Se_{0.875}Cl_{0.125}$ around the Fermi level obtained by the standard DFT method. For Bi_2O_2Se, the valence bands from 4 to 5.53 eV are mainly composed of Se 4*p* orbitals hybridized with O 2*p* and Bi 6*s* orbitals, while the conduction bands from 6.02 to 8 eV are mainly composed of Bi 6*p* and O 2*p* orbitals. The bandgap between the maximum value of the valence band and the minimum value of the conduction band is 0.49 eV, which is similar to the theoretical values of 0.41 eV [45], 0.43 eV [46], and 0.472 eV [47]. Figure 2b shows the DOS distribution of $Bi_2O_2Se_{0.875}Cl_{0.125}$, revealing that many electrons are distributed at the Fermi level. These features indicate that $Bi_2O_2Se_{0.875}Cl_{0.125}$ has metallic properties that differ from the results reported by Tan et al. [48]. This is mainly due to the fact that our doping concentration of 2.5% is far greater than the solubility limit of 1.5% in the experimental literature.
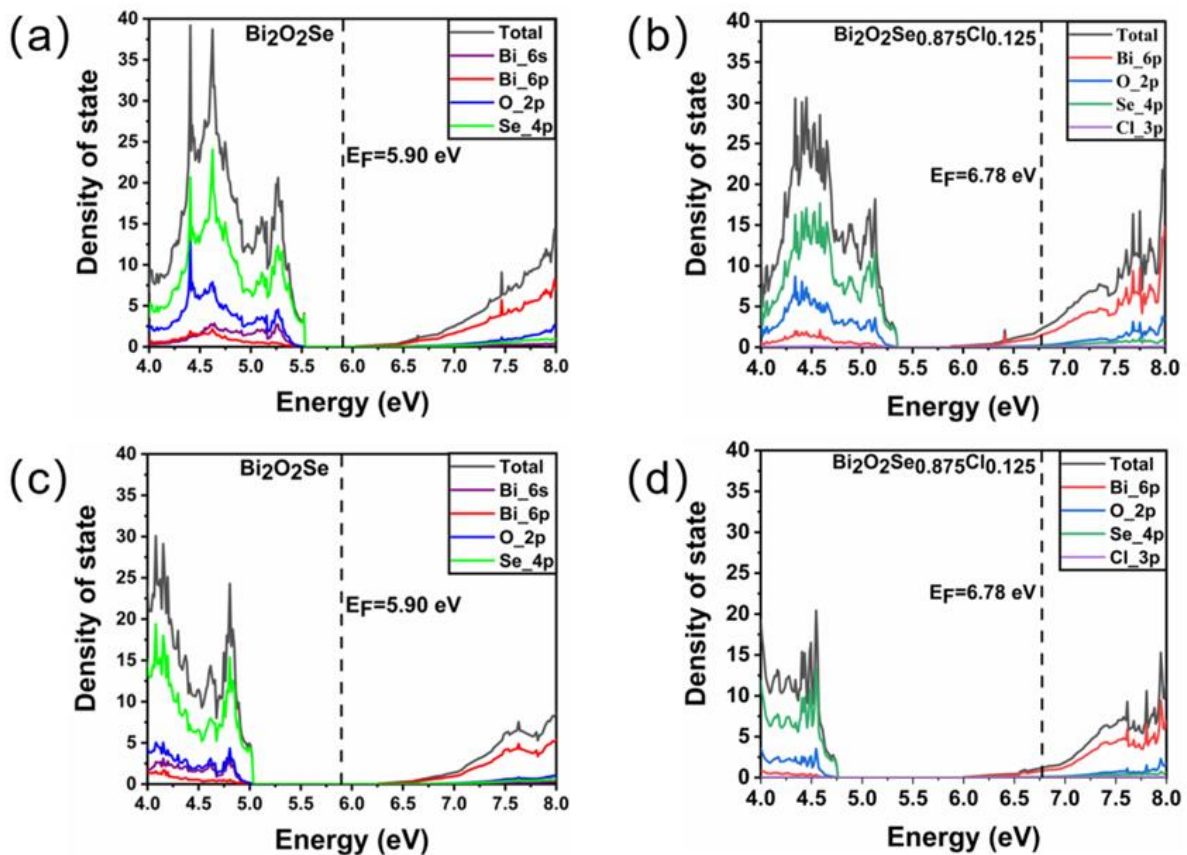

Figure 2. The total and projected density of state distribution for Bi_2O_2Se and $Bi_2O_2Se_{0.875}Cl_{0.125}$ obtained by (**a**,**b**) standard DFT method and (**c**,**d**) hybrid DFT method. The E_F denotes the Fermi energy.

As we know, the standard DFT method severely underestimates the bandgap of materials. In order to obtain a more accurate bandgap, we use the hybrid DFT method to further calculate the DOS distribution of Bi_2O_2Se before and after Cl doping. Figure 2c,d show the DOS distribution of Bi_2O_2Se before and after Cl doping, respectively. For Bi_2O_2Se, the calculated band gap between the maximum of the valence band and the minimum of the conduction band is 1.05 eV, which is similar to other calculated hybrid DFT results of 0.9 eV [49], 0.99 eV [50] and 1.01 eV [51]. For $Bi_2O_2Se_{0.875}Cl_{0.125}$, it can be seen that as compared with the standard DFT method, the hybrid DFT method obtains a more delocalized electron distribution, and a certain number of electrons still distribute on the Fermi level, i.e., the doped Bi_2O_2Se exhibits metallic properties.

3.3. Thermal Transport Properties of Bi_2O_2Se and $Bi_2O_2Se_{0.875}Cl_{0.125}$

3.3.1. Relaxation Time and Electrical Conductivity of Pure and Cl-Doped Bi_2O_2Se

When calculating thermoelectric properties such as the Seebeck coefficient, electrical conductivity, and thermal conductivity, two variables, i.e., carrier concentration and relaxation time, must be determined first, both of which are functions of temperature. Considering the phenomenon that Cl doping results in metallic behavior in Bi_2O_2Se similar to that of W doping [52], we refer to the carrier concentration of W-doped Bi_2O_2Se for our calculation. Therefore, the carrier concentration of pure and Cl-doped Bi_2O_2Se is $n = 1.36 \times 10^{19}$ cm^{-3} and $n = 1.56 \times 10^{19}$ cm^{-3}, respectively. The relaxation time τ for Bi_2O_2Se at 300 K can be obtained with the following formula [53]:

$$\tau = \frac{\mu m^*}{e},\tag{1}$$

where m^* is the effective mass and μ is the carrier mobility. Employing $m^* = 0.33\ m_0$ and $\mu = 80$ cm^{2}V^{-1}s^{-1} at 300 K, as reported by Gao et al. [52], we obtain $\tau = 1.5 \times 10^{-14}$ s at 300 K for Bi_2O_2Se, which is comparable with the experimental result of 1.2×10^{-14} s reported by Pan et al. [54]. As for $Bi_2O_2Se_{0.875}Cl_{0.125}$, referring to the relaxation time of W-doped Bi_2O_2Se (1.9×10^{-14} s) [52] and other metals (0.31×10^{-14} s~2.2×10^{-14} s) [55], an approximate relaxation time τ of 1×10^{-14} s at 300 K is employed.

The relaxation time τ for Bi_2O_2Se and $Bi_2O_2Se_{0.875}Cl_{0.125}$ at different temperatures can be calculated by the following equation [56]:

$$\tau = \frac{C}{Tn^{\frac{1}{3}}}\tag{2}$$

where n is the carrier concentration, T is the temperature, and C is a constant. According to the experimental literature [52], carrier concentrations are fixed at 1.36×10^{19} cm^{-3} for Bi_2O_2Se and 1.56×10^{19} cm^{-3} for $Bi_2O_2Se_{0.875}Cl_{0.125}$, which are also employed in other investigations [23,56–59]. Taking the relaxation time τ calculated at 300 K into Equation (2), the constants C are determined to be 1.78×10^{-10} sKcm^{-1} for Bi_2O_2Se and 8.21×10^{-10} sKcm^{-1} for $Bi_2O_2Se_{0.875}Cl_{0.125}$. Then, by substituting the constants C and n into Equation (2), the relaxation time τ at different temperatures is obtained. The calculated results are plotted in Figure 3a. It is shown that the relaxation time τ is dependent on the temperature and becomes smaller with increasing temperature.

Based on the determined relaxation time and carrier concentration, we further calculate the electrical conductivity σ of Bi_2O_2Se before and after Cl doping. Figure 3b shows the temperature-dependent electrical conductivity σ of Bi_2O_2Se and $Bi_2O_2Se_{0.875}Cl_{0.125}$. For Bi_2O_2Se, the calculated electrical conductivity σ decreases with increasing temperature, which is consistent with the experimental literature [52]. However, our results differ from those of Rurova et al. [60], due to the reason that the carrier concentration is fixed in our calculations while dependent on the temperature in the work of Rurova et al. As for $Bi_2O_2Se_{0.875}Cl_{0.125}$, the electrical conductivity σ is as high as 9390 S/cm at 300 K, which is 26 times larger than the value of 358.5 S/cm for Bi_2O_2Se. Experimentally, the Bi_2O_2Se

sample (σ = 175 S/cm) was prepared by the exfoliation technique [52], which may produce defects and influence its physical properties [61]. In addition, the dissolution limit of Cl in Bi_2O_2Se reported in the literature is 1.5% [48], while the dopant concentration considered in this work is much higher, i.e., 2.5%. Although the dopant concentration considered in this work is higher than the experimental dissolution limit, the dissolution limit can be raised by techniques such as tuning the experimental temperature and powder size of the samples [37–39]. Therefore, the presented results will provide a theoretical reference for further related experimental research.
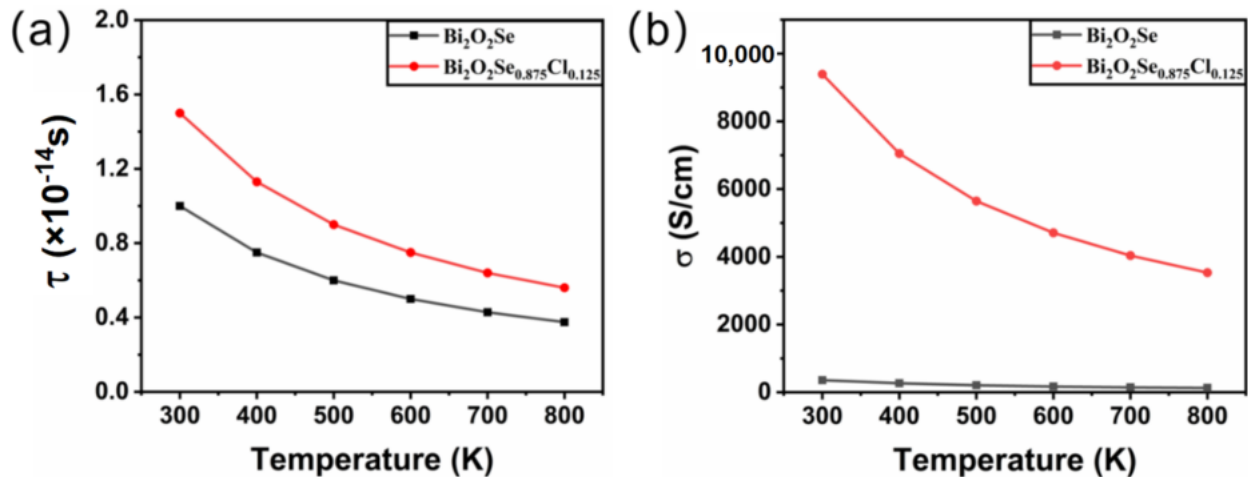

Figure 3. The calculated (**a**) relaxation time and (**b**) electrical conductivity for Bi_2O_2Se and $Bi_2O_2Se_{0.875}Cl_{0.125}$ as a function of temperature.

3.3.2. Seebeck Coefficient and Power Factor of Bi_2O_2Se and $Bi_2O_2Se_{0.875}Cl_{0.125}$

The Seebeck coefficient S is an essential parameter for predicting the thermoelectric performance of materials. It is mainly determined by the thermal electromotive force ($\triangle V$) and the temperature difference ($\triangle T$) and can be expressed as [62]:

$$S = \frac{\triangle V}{\triangle T} \tag{3}$$

Figure 4a presents the variation of the Seebeck coefficient S with temperature for Bi_2O_2Se and $Bi_2O_2Se_{0.875}Cl_{0.125}$. It is shown that the Seebeck coefficients S of Bi_2O_2Se and $Bi_2O_2Se_{0.875}Cl_{0.125}$ are both negative, indicating that electrons are the dominant charge carriers. Due to the increase in free electron concentration, Cl doping leads to a significant decrease in the absolute value of the Seebeck coefficient S of Bi_2O_2Se. In addition, as the temperature increases, the absolute Seebeck coefficient S increases for both Bi_2O_2Se and $Bi_2O_2Se_{0.875}Cl_{0.125}$. For Bi_2O_2Se, the absolute Seebeck coefficient S increases from 87.6 μV/K at room temperature to 177 μV/K at 800 K; for $Bi_2O_2Se_{0.875}Cl_{0.125}$, the absolute Seebeck coefficient S increases from 23.8 μV/K at room temperature to 59.7 μV/K at 800 K.

Based on the calculated electrical conductivity σ and Seebeck coefficient S, we further calculate the power factor PF of Bi_2O_2Se before and after Cl doping using the following formula:

$$PF = S^2\sigma \tag{4}$$

Figure 4b shows the temperature-dependent power factors (PFs) of Bi_2O_2Se and $Bi_2O_2Se_{0.875}Cl_{0.125}$. It is evident that the PF values for Bi_2O_2Se and $Bi_2O_2Se_{0.875}Cl_{0.125}$ increase with increasing temperature. In addition, Cl doping significantly enhances the PF of Bi_2O_2Se. For example, at a temperature of 800 K, the power factor PF of $Bi_2O_2Se_{0.875}Cl_{0.125}$ is 12.59 mW/m K^2, which is 3.04 times that of pure Bi_2O_2Se (4.14 mW/m K^2).
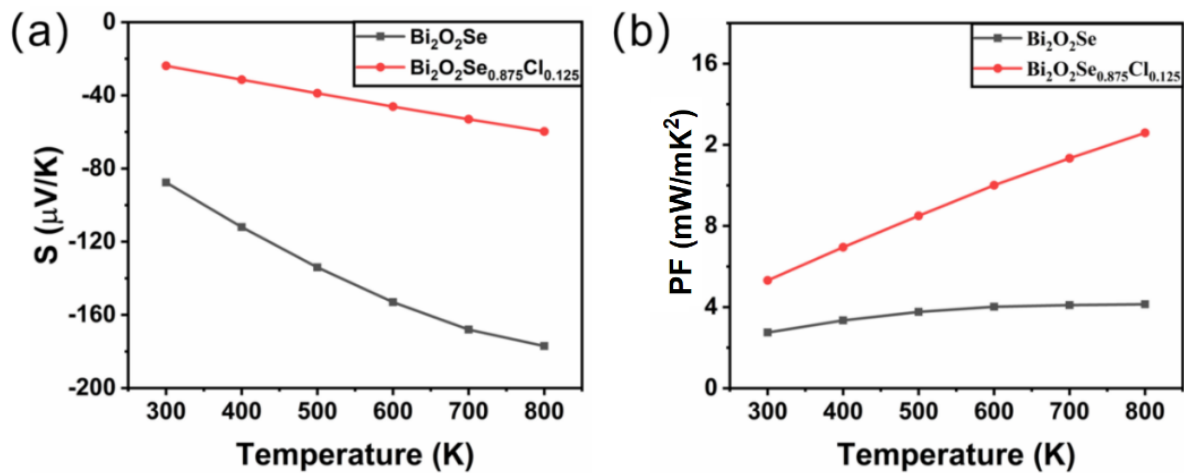
Figure 4. The calculated (**a**) Seebeck coefficient and (**b**) power factor for Bi_2O_2Se and $Bi_2O_2Se_{0.875}Cl_{0.125}$ as a function of temperature.

3.3.3. Thermal Conductivity and Figure of Merit *ZT* of Pure and Cl-Doped Bi_2O_2Se

The thermal conductivity of a crystal is determined by the combined effects of electronic thermal conductivity and lattice thermal conductivity, i.e.,

$$\kappa = \kappa_e + \kappa_l \tag{5}$$

The Wiedemann–Franz law [35,63,64] can be applied to calculate the electronic thermal conductivity of materials, i.e.,

$$\kappa_e = L\sigma T \tag{6}$$

Here, L represents the Lorenz constant (2.4×10^{-8} $W\Omega K^{-2}$). The temperature-dependent behavior of electronic thermal conductivity is shown in Figure 5a. It is observed that the electronic thermal conductivity of Bi_2O_2Se and $Bi_2O_2Se_{0.875}Cl_{0.125}$ increases with increasing temperature. Moreover, the electronic thermal conductivity of $Bi_2O_2Se_{0.875}Cl_{0.125}$ is significantly higher than that of Bi_2O_2Se. For instance, at a temperature of 800 K, the calculated value of $Bi_2O_2Se_{0.875}Cl_{0.125}$ is 6.78 W/mK, which is 27.12 times larger than that of Bi_2O_2Se (0.25 W/mK). This can be attributed to the remarkable improvement in the electronic conductivity of Bi_2O_2Se caused by Cl doping.

The Slack equation [36] can be used to calculate the lattice thermal conductivity κ_l:

$$\kappa_l = A \cdot \frac{\overline{M}\Theta^3\delta}{\gamma^2 T n^{\frac{2}{3}}} \tag{7}$$

The Slack model has been demonstrated to provide lattice thermal conductivity results that agree well with experimental measurements and has been extensively used in the calculation of lattice thermal conductivity for materials [49,65–67]. Here, A is a constant, and the calculation formula is given by:

$$A = 2.43 * \frac{10^{-6}}{1 - \frac{0.514}{\gamma} + \frac{0.228}{\gamma^2}} \tag{8}$$

In this equation, $\overline{M}$ represents the average atomic mass, δ^3 is the volume of each atom, γ is the Grüneisen parameter, Θ is the Debye temperature, and T is the absolute temperature. Figure 5b shows the temperature-dependent behavior of the lattice thermal conductivity κ_l. It is observed that the lattice thermal conductivity of both Bi_2O_2Se and $Bi_2O_2Se_{0.875}Cl_{0.125}$ decreases with increasing temperature. For Bi_2O_2Se, the calculated lattice thermal conductivity κ_l at 300 K is 1.68 W/mK, which agrees well with the experimental data of κ = 1.8 W/mK and other calculated results of κ = 1.2 W/mK [51]. Furthermore,

Cl doping reduces the lattice thermal conductivity of Bi_2O_2Se. For example, the calculated lattice thermal conductivity of $Bi_2O_2Se_{0.875}Cl_{0.125}$ at 300 K is 1.29 W/mK, which is 23.21% smaller than that of Bi_2O_2Se (1.68 W/mK). This is mainly due to the low elastic constants of $Bi_2O_2Se_{0.875}Cl_{0.125}$. The reduced lattice thermal conductivity will be beneficial for suppressing heat transfer and minimizing thermal energy loss.
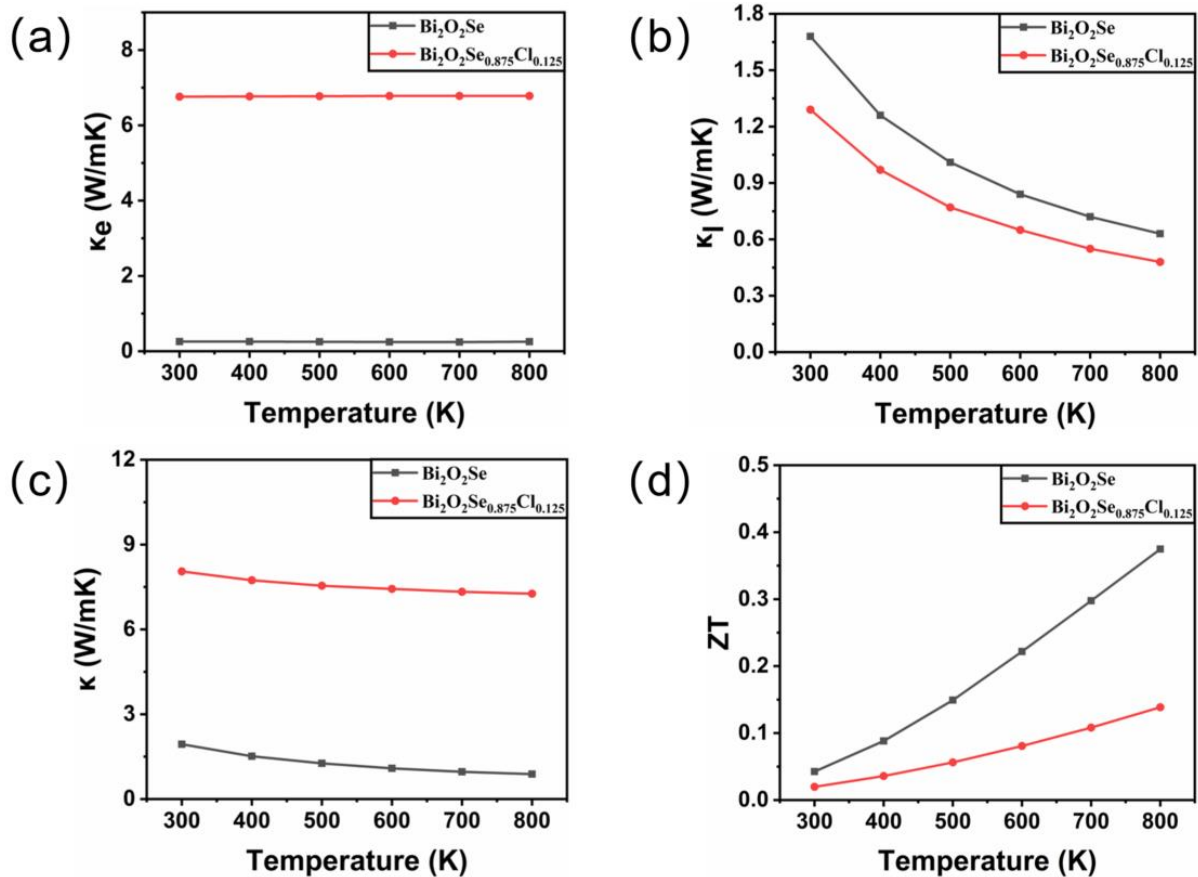

Figure 5. The calculated (**a**) electronic thermal conductivity κ_e, (**b**) lattice thermal conductivity κ_l, (**c**) total thermal conductivity κ, and (**d**) figure of merit *ZT* for Bi_2O_2Se and $Bi_2O_2Se_{0.875}Cl_{0.125}$ as a function of temperature.

Combining the calculated electronic thermal conductivity κ_e and lattice thermal conductivity κ_l into Equation (5), the thermal conductivity of Bi_2O_2Se before and after Cl doping can be obtained, as depicted in Figure 5c. It is shown that Cl doping results in an increase in the thermal conductivity of Bi_2O_2Se, due to a substantial increase in the electronic thermal conductivity κ_e.

The *ZT* value of Bi_2O_2Se before and after Cl doping can be obtained by the following formula [7]:

$$ZT = \frac{S^2 \sigma T}{\kappa} \qquad (9)$$

as shown in Figure 5d. At 300 K, the calculated *ZT* value for Bi_2O_2Se is 0.04, which is in good agreement with the reported values of 0.05 by Gao et al. [52] and 0.045 by Song et al. [22]. Furthermore, the *ZT* values of both Bi_2O_2Se and $Bi_2O_2Se_{0.875}Cl_{0.125}$ increase with increasing temperature. However, the *ZT* value of $Bi_2O_2Se_{0.875}Cl_{0.125}$ is lower than that of Bi_2O_2Se due to the introduction of Cl dopants. This is mainly due to the decrease in the Seebeck coefficient caused by the introduction of Cl dopants. The presented results thus suggest that Cl doping is not beneficial for improving the thermoelectric properties of Bi_2O_2Se.

4. Conclusions

In summary, the effects of Cl doping on the structural, electronic, and thermoelectric properties of Bi_2O_2Se are investigated by combining the DFT method and semi-classical Boltzmann theory. The results indicate that Cl doping leads to a 0.76% volume expansion of Bi_2O_2Se and a significant shift of the Fermi level into the conduction band, resulting in metallic properties. Additionally, Cl doping can introduce extra electrons, resulting in a higher electrical conductivity (σ), a lower absolute Seebeck coefficient (S), and a higher power factor (*PF*). These findings suggest that Cl doping can optimize the thermoelectric properties of Bi_2O_2Se. However, the introduction of Cl dopants in Bi_2O_2Se results in a significant increase in the absolute value of the Seebeck coefficient, leading to a notable decrease in its *ZT* value. In conclusion, Cl doping can affect the thermoelectric properties of Bi_2O_2Se significantly, providing insights for further related experimental and theoretical studies.

Conflicts of Interest: The authors declare no conflict of interest.

References

1. Abdalla, A.M.; Hossain, S.; Nisfindy, O.B.; Azad, A.T.; Dawood, M.; Azad, A.K. Hydrogen production, storage, transportation and key challenges with applications: A review. *Energy Convers. Manag.* **2018**, *165*, 602–627. [CrossRef]
2. Ren, J.; Musyoka, N.M.; Langmi, H.W.; Mathe, M.; Liao, S. Current research trends and perspectives on materials-based hydrogen storage solutions: A critical review. *Int. J. Hydrogen Energy* **2017**, *42*, 289–311. [CrossRef]
3. Yu, X.; Tang, Z.; Sun, D.; Ouyang, L.; Zhu, M. Recent advances and remaining challenges of nanostructured materials for hydrogen storage applications. *Prog. Mater. Sci.* **2017**, *88*, 1–48. [CrossRef]
4. Liu, W.; Jie, Q.; Kim, H.S.; Ren, Z. Current progress and future challenges in thermoelectric power generation: From materials to devices. *Acta Mater.* **2015**, *87*, 357–376. [CrossRef]
5. Zhu, H.; Xiao, C.; Xie, Y. Design of Highly Efficient Thermoelectric Materials: Tailoring Reciprocal-Space Properties by Real-Space Modification. *Adv. Mater.* **2018**, *30*, e1802000. [CrossRef] [PubMed]
6. Boukai, A.I.; Bunimovich, Y.; Tahir-Kheli, J.; Yu, J.K.; Goddard, W.A., 3rd; Heath, J.R. Silicon nanowires as efficient thermoelectric materials. *Nature* **2008**, *451*, 168–171. [CrossRef] [PubMed]
7. Snyder, G.J.; Toberer, E.S. Complex thermoelectric materials. *Nat. Mater.* **2008**, *7*, 105–114. [CrossRef]
8. Wang, N.; Li, M.; Xiao, H.; Gong, H.; Liu, Z.; Zu, X.; Qiao, L. Optimizing the thermoelectric transport properties of Bi_2O_2Se monolayer via biaxial strain. *Phys. Chem. Chem. Phys.* **2019**, *21*, 15097–15105. [CrossRef]
9. Heremans, J.P.; Jovovic, V.; Toberer, E.S.; Saramat, A.; Kurosaki, K.; Charoenphakdee, A.; Yamanaka, S.; Snyder, G.J. Enhancement of Thermoelectric Efficiency in PbTe by Distortion of the Electronic Density of States. *Science* **2008**, *321*, 554–557. [CrossRef]
10. Tan, G.; Zhao, L.D.; Kanatzidis, M.G. Rationally Designing High-Performance Bulk Thermoelectric Materials. *Chem. Rev.* **2016**, *116*, 12123–12149. [CrossRef]
11. Hochbaum, A.I.; Chen, R.; Delgado, R.D.; Liang, W.; Garnett, E.C.; Najarian, M.; Majumdar, A.; Yang, P. Enhanced thermoelectric performance of rough silicon nanowires. *Nature* **2008**, *451*, 163–167. [CrossRef]
12. Lu, W.; Ji, Z.; Pfeiffer, L.; West, K.W.; Rimberg, A.J. Real-time detection of electron tunnelling in a quantum dot. *Nature* **2003**, *423*, 422–425. [CrossRef]
13. Heikes, R.; Ure, R., Jr. *Thermo Electricity: Science and Engineering Intersciences*; Interscience Publishers: New York, NY, USA, 1961; Volume 285, p. 40.
14. Gelbstein, Y.; Dashevsky, Z.; Dariel, M.P. High performance n-type PbTe-based materials for thermoelectric applications. *Phy. B* **2005**, *363*, 196–205. [CrossRef]

15. Fleischmann, H.; Luy, H.; Rupprecht, J. Neuere Untersuchungen an halbleitenden IV VI-1 V VI2-Mischkristallen. *Zeitschri' Für Naturforschung A* **1963**, *18*, 646–649. [CrossRef]

16. Wood, C. Materials for thermoelectric energy conversion. *Rep. Prog. Phys.* **1988**, *51*, 459–539. [CrossRef]

17. Hsu, K.F.; Loo, S.; Guo, F.; Chen, W.; Dyck, J.S.; Uher, C.; Hogan, T.; Polychroniadis, E.K.; Kanatzidis, M.G. Cubic AgPb(m)SbTe(2+m): Bulk thermoelectric materials with high figure of merit. *Science* **2004**, *303*, 818–821. [CrossRef] [PubMed]

18. Rosi, F.; Hockings, E.; Lindenblad, N. Semiconducting materials for thermoelectric power generation. *RCA Rev.* **1961**, *22*, 82–121.

19. Zhan, B.; Liu, Y.; Tan, X.; Lan, J.l.; Lin, Y.h.; Nan, C.W.; Zhou, X.D. Enhanced Thermoelectric Properties of Bi_2O_2Se Ceramics by Bi Deficiencies. *J. Am. Ceram. Soc.* **2015**, *98*, 2465–2469. [CrossRef]

20. Li, Y.; Huo, H.; Huang, H.; Guo, K.; Yang, X.; Xing, J.; Luo, J.; Rao, G.-H.; Zhao, J.-T. Optimization of electrical and thermal transport properties of layered Bi_2O_2Se via Nb doping. *J. Mater. Sci* **2021**, *56*, 12732–12739. [CrossRef]

21. Hong, H.Y.; Kim, D.H.; Won, S.O.; Park, K. Enhancement of the thermoelectric performance of n−type Bi_2O_2Se by Ce^{4+} doping. *J. Mater. Res. Technol.* **2021**, *15*, 4161–4172. [CrossRef]

22. Song, C.; Song, Y.; Pan, L.; Chen, C.; Zong, P.; Wang, Y. Thermoelectric properties of Bi_2TiO_2Se with the shear exfoliation-restacking process. *J. Alloys Compd.* **2022**, *892*, 162147. [CrossRef]

23. Yang, N.; Pan, L.; Chen, C.; Wang, Y. Effects of Sb-doping on the electron-phonon transport properties of Bi_2O_2Se. *J. Alloys Compd.* **2021**, *858*, 157748. [CrossRef]

24. Pan, L.; Zhao, Z.; Yang, N.; Xing, W.; Zhang, J.; Liu, Y.; Chen, C.; Li, D.; Wang, Y. Effects of sulfur substitution for oxygen on the thermoelectric properties of Bi_2O_2Se. *J. Eur. Ceram. Soc.* **2020**, *40*, 5543–5548. [CrossRef]

25. Fu, Z.; Jiang, J.-L.; Dong, S.-T.; Yu, M.-C.; Zhao, L.; Wang, L.; Yao, S.-H. Effects of Zr substitution on structure and thermoelectric properties of Bi_2O_2Se. *J. Mater. Res. Thechnol.* **2022**, *21*, 640–647. [CrossRef]

26. Song, C.; Zhou, H.; Gu, Y.; Pan, L.; Chen, C.; Wang, Y. Enhanced thermoelectric properties of Bi_2O_2Se by $Bi_2Te_{2.7}Se_{0.3}$ addition. *J. Alloys Compd.* **2023**, *930*, 167439. [CrossRef]

27. Wang, S.; Su, L.; Qiu, Y.; Xiao, Y.; Zhao, L.-D. Enhanced thermoelectric performance in Cl-doped $BiSbSe_3$ with optimal carrier concentration and effective mass. *J. Mater. Sci. Technol.* **2021**, *70*, 67–72. [CrossRef]

28. Tan, G.; Hao, S.; Zhao, J.; Wolverton, C.; Kanatzidis, M.G. High thermoelectric performance in electron-doped $AgBi_3S_5$ with ultralow thermal conductivity. *J. Am. Chem. Soc.* **2017**, *139*, 6467–6473. [CrossRef]

29. Zhang, Q.; Lan, Y.; Yang, S.; Cao, F.; Yao, M.; Opeil, C.; Broido, D.; Chen, G.; Ren, Z. Increased thermoelectric performance by Cl doping in nanostructured $AgPb_{18}SbSe_{20−x}Cl_x$. *Nano Energy* **2013**, *2*, 1121–1127. [CrossRef]

30. Kresse, G.; Furthmu¨ller, J. Efficient iterative schemes for ab initio total-energy calculations using a plane-wave basis set. *Phys. Rev. B* **1996**, *54*, 11169. [CrossRef]

31. Kresse, G.; Joubert, D. From ultrasoft pseudopotentials to the projector augmented-wave method. *Phys. Rev. B* **1999**, *59*, 1758. [CrossRef]

32. Qiao, L.; Zhang, S.; Xiao, H.Y.; Singh, D.J.; Zhang, K.H.L.; Liu, Z.J.; Zu, X.T.; Li, S. Orbital controlled band gap engineering of tetragonal BiFeO3 for optoelectronic applications. *J. Mater. Chem. C* **2018**, *6*, 1239–1247. [CrossRef]

33. Heyd, J.; Scuseria, G.E.; Ernzerhof, M. Hybrid functionals based on a screened Coulomb potential. *J. Chem. Phys.* **2003**, *118*, 8207–8215. [CrossRef]

34. Monkhorst, H.J.; Pack, J.D. Special points for Brillouin-zone integrations. *Phys. Rev. B* **1976**, *13*, 5188–5192. [CrossRef]

35. Madsen, G.K.H.; Singh, D.J.; BoltzTra, P. A code for calculating band-structure dependent quantities. *Comput. Phys. Commun.* **2006**, *175*, 67–71. [CrossRef]

36. Morelli, D.T.; Slack, G.A. *High Lattice Thermal Conductivity of Solids*; Springer: New York, NY, USA, 2006; pp. 37–68.

37. Serier, H.; Gaudon, M.; Ménétrier, M. Al-doped ZnO powdered materials: Al solubility limit and IR absorption properties. *Solid State Sci.* **2009**, *11*, 1192–1197. [CrossRef]

38. Martínez, V.d.P.; Aguilar, C.; Marín, J.; Ordoñez, S.; Castro, F. Mechanical alloying of Cu–Mo powder mixtures and thermodynamic study of solubility. *Mater. Lett.* **2007**, *61*, 929–933. [CrossRef]

39. Zhou, E.; Suryanarayana, C.; Froes, F.S. Effect of premilling elemental powders on solid solubility extension of magnesium in titanium by mechanical alloying. *Mater. Lett.* **1995**, *23*, 27–31. [CrossRef]

40. Liu, R.; Lan, J.-L.; Tan, X.; Liu, Y.-C.; Ren, G.-K.; Liu, C.; Zhou, Z.-F.; Nan, C.-W.; Lin, Y.-H. Carrier concentration optimization for thermoelectric performance enhancement in n-type Bi_2O_2Se. *J. Eur. Ceram. Soc.* **2018**, *38*, 2742–2746. [CrossRef]

41. Wu, J.; Tan, C.; Tan, Z.; Liu, Y.; Yin, J.; Dang, W.; Wang, M.; Peng, H. Controlled Synthesis of High-Mobility Atomically Thin Bismuth Oxyselenide Crystals. *Nano Lett.* **2017**, *17*, 3021–3026. [CrossRef]

42. Boiler, I. Die Kristallstruktur von Bi_2O_2Se. *Monatsh. Chem.* **1973**, *104*, 916–919. [CrossRef]

43. Chen, Q.; Zhang, P.; Qin, M.; Lou, Z.; Gong, L.; Xu, J.; Kong, J.; Yan, H.; Gao, F. Effect of La^{3+}, Ag^+ and Bi^{3+} doping on thermoelectric properties of $SrTiO_3$: First-principles investigation. *Ceram. Int.* **2022**, *48*, 13803–13816. [CrossRef]

44. Wu, J.; Yuan, H.; Meng, M.; Chen, C.; Sun, Y.; Chen, Z.; Dang, W.; Tan, C.; Liu, Y.; Yin, J.; et al. High electron mobility and quantum oscillations in non-encapsulated ultrathin semiconducting Bi_2O_2Se. *Nat. Commun.* **2017**, *12*, 530–534. [CrossRef] [PubMed]

45. Hu, K.; Han, J.; Xu, B.; Lin, Y.H. Thermoelectric power factor of doped Bi_2O_2Se: A computational study. *Phys. Chem. Chem. Phys.* **2020**, *22*, 27096–27104. [CrossRef]

46. Li, J.Q.; Cheng, C.; Duan, M.Y. The electronic and optical properties of multi-layer Bi_2O_2X (X = S, Se, Te) by first-principles calculations. *Appl. Surf. Sci.* **2023**, *618*, 156541. [CrossRef]

47. Wang, Y.; Xu, B.; Yu, G.; Zhang, J.; Ma, S.; Yuan, S.; Sun, T.; Wang, Y. Electronic structure and thermoelectric properties of Bi_2O_2Se with GGA and TB-mBJ potentials. *Jpn. J. Appl. Phys.* **2019**, *58*, 015501. [CrossRef]

48. Tan, X.; Lan, J.-l.; Ren, G.; Liu, Y.; Lin, Y.-H.; Nan, C.-W. Enhanced thermoelectric performance of n-type Bi_2O_2Se by Cl-doping at Se site. *J. Am. Ceram. Soc.* **2017**, *100*, 1494–1501. [CrossRef]

49. Li, M.; Wang, N.; Jiang, M.; Xiao, H.; Zhang, H.; Liu, Z.; Zu, X.; Qiao, L. Improved thermoelectric performance of bilayer Bi_2O_2Se by the band convergence approach. *J. Mater. Chem. C* **2019**, *7*, 11029–11039. [CrossRef]

50. Liu, J.; Tian, L.; Mou, Y.; Jia, W.; Zhang, L.; Liu, R. Electronic and mechanical property of high electron mobility semiconductor Bi_2O_2Se. *J. Alloys Compd.* **2018**, *764*, 674–678. [CrossRef]

51. Zhu, X.L.; Liu, P.F.; Xie, G.; Wang, B.T. First-principles study of thermal transport properties in the two- and three-dimensional forms of Bi_2O_2Se. *Phys. Chem. Chem. Phys.* **2019**, *21*, 10931–10938. [CrossRef]

52. Gao, Y.; Wang, Y.; Pan, L.; Chen, C.; Zong, P.; Wang, Y. Enhancing thermoelectric performance of Bi_2O_2Se by W-doping with the shear exfoliation-restacking process. *Mater. Lett.* **2022**, *308*, 131291. [CrossRef]

53. Bardeen, J.; Shockley, W. Deformation Potentials and Mobilities in Non-Polar Crystals. *Phys. Rev.* **1950**, *80*, 72–80. [CrossRef]

54. Pan, L.; Zhang, J.; Chen, C.; Wang, Y. Enhanced thermoelectric properties of highly textured Bi_2O_2-Se^{1+} with liquid-phase mechanical exfoliation. *Scr. Mater.* **2020**, *178*, 376–381. [CrossRef]

55. Smith, J.B.; Ehrenreich, H. Frequency dependence of the optical relaxation time in metals. *Phys. Rev. B* **1982**, *25*, 923–930. [CrossRef]

56. Guo, D.; Hu, C.; Xi, Y.; Zhang, K. Strain Effects To Optimize Thermoelectric Properties of Doped Bi_2O_2Se via Tran–Blaha Modified Becke–Johnson Density Functional Theory. *J. Phys. Chem. C* **2013**, *117*, 21597–21602. [CrossRef]

57. Sikam, P.; Moontragoon, P.; Ikonic, Z.; Kaewmaraya, T.; Thongbai, P. The study of structural, morphological and optical properties of (Al, Ga)-doped ZnO: DFT and experimental approaches. *Appl. Surf. Sci.* **2019**, *480*, 621–635. [CrossRef]

58. Pei, Y.; Wang, H.; Snyder, G.J. Band engineering of thermoelectric materials. *Adv. Mater.* **2012**, *24*, 6125–6135. [CrossRef]

59. Zhang, J.; Wu, D.; He, D.; Feng, D.; Yin, M.; Qin, X.; He, J. Extraordinary Thermoelectric Performance Realized in n-Type PbTe through Multiphase Nanostructure Engineering. *Adv. Mater.* **2017**, *29*, 1703148. [CrossRef]

60. Ruleova, P.; Drasar, C.; Lostak, P.; Li, C.P.; Ballikaya, S.; Uher, C. Thermoelectric properties of Bi_2O_2Se. *Mater. Chem. Phys.* **2010**, *119*, 299–302. [CrossRef]

61. Islam, M.A.; Serles, P.; Kumral, B.; Demingos, P.G.; Qureshi, T.; Meiyazhagan, A.; Puthirath, A.B.; Abdullah, M.S.B.; Faysal, S.R.; Ajayan, P.M.; et al. Exfoliation Mechanisms of 2D Materials and Their Applications. *Appl. Phys. Rev.* **2022**, *9*, 041301. [CrossRef]

62. Kim, M.; Park, D.; Kim, J. Enhancement of Bi_2O_2Se thermoelectric power factor via Nb doping. *J. Alloys Compd.* **2021**, *851*, 156905. [CrossRef]

63. Stojanovic, N.; Maithripala, D.H.S.; Berg, J.M.; Holtz, M. Thermal conductivity in metallic nanostructures at high temperature: Electrons, phonons, and the Wiedemann-Franz law. *Phys. Rev. B* **2010**, *82*, 075418. [CrossRef]

64. Wang, D.; He, W.; Chang, C.; Wang, G.; Wang, J.; Zhao, L.-D. Thermoelectric transport properties of rock-salt SnSe: First-principles investigation. *J. Mater. Chem. C* **2018**, *6*, 12016–12022. [CrossRef]

65. Li, Y.; Wang, J.; Wang, J. Approaching extremely low thermal conductivity by crystal structure engineering in $Mg_2A_{14}Si_5O_{18}$. *J. Mater. Res.* **2015**, *30*, 3729–3739. [CrossRef]

66. Li, Y.; Luo, Y.; Tian, Z.; Wang, J.; Wang, J. Theoretical exploration of the abnormal trend in lattice thermal conductivity for monosilicates RE_2SiO_5 (RE = Dy, Ho, Er, Tm, Yb and Lu). *J. Eur. Ceram. Soc.* **2018**, *38*, 3539–3546. [CrossRef]

67. Shindé, S.L.; Goela, J. (Eds.) *High Thermal Conductivity Materials*; Springer: New York, NY, USA, 2006; p. 91.